NANO LETTERS

pubs.acs.org/NanoLett Letter

Discovery of a Stripe Phase in an Elemental Solid

Maksim Litskevich,[†] Md Shafayat Hossain,*[,†] Yang Fu,[†] Hu Miao, Yuxiao Jiang, Guangming Cheng, Pengcheng Chen, Qi Zhang, Zi-Jia Cheng, Raul Acevedo-Esteves, Christie Nelson, Haozhe Wang, Jose L. Gonzalez Jimenez, Brian Casas, Xiaoxiong Liu, Stepan S. Tsirkin, Kouta Dagnino, Songbo Zhang, Chia-Hsiu Hsu, Sen Shao, Shaogang Xu, Tyler A. Cochran, Xian P. Yang, Hu Xu, Jiaxin Yin, Yaroslav A. Gerasimenko, Weiwei Xie, Nan Yao, Luis Balicas, Guoqing Chang, Titus Neupert, Hechang Lei, and M. Zahid Hasan*

Cite This: https://doi.org/10.1021/acs.nanolett.5c01695 Read Online

ACCESS | Metrics & More | Article Recommendations | Supporting Information

ABSTRACT: Translational symmetry breaking is foundational to condensed matter physics because it is associated with crystal formation. At much lower energy scales, the breaking of crystalline translational symmetry can be driven by electronic, rather than ionic, degrees of freedom and may give rise to stripe order, a unidirectional ordered state. Such symmetry breaking has been seen in two-dimensional and strongly correlated systems. Here, for the first time, we report the observation of stripe order in an elemental solid, tellurium. Through topographic and spectroscopic imaging, we discover a commensurate 4 × 1 stripe phase. Surprisingly, this exotic order is so robust that it survives close to room temperature. Notably, our diffraction experiments confirm the bulk nature of the stripe order, showing the minuteness of potential lattice distortion associated with the order. Our discovery of the stripe order in tellurium opens new windows to understanding the spontaneous symmetry breaking in elemental solids.

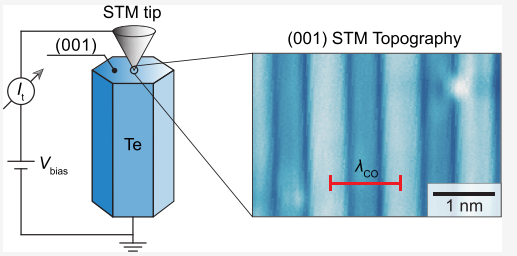

KEYWORDS: *phase transitions, charge order, semiconductors, chiral crystals, scanning tunneling microscopy, X-ray diffraction*

Symmetry breaking[1] is a foundational concept in the classification of matter. A typical symmetry breaking phenomenon involves the development of an electronic charge order that manifests as a periodic modulation in the charge density.[2,3] When the electronic charge-ordered state spontaneously breaks the symmetry of the underlying crystal lattice, stripe phases can emerge.[4−7] Stripe phases have been identified in doped Mott insulators,[8−12] pnictide superconductors[13−16] and correlated two-dimensional (2D) electronic systems.[17−21] Here, we report the observation of a stripe phase in single-crystalline tellurium (Te). Te is a strong spin−orbit material and a Weyl semiconductor candidate with interests in nanoelectronics, spintronics, and chirality-driven applications.[22−34] Exhibiting diverse electrical properties, Te stands out for its high-performance thermoelectricity[35,36] and strong piezoelectric characteristics.[37,38] In addition, 2D tellurium nanoflakes exhibit a band gap that varies with thickness,[39] along with a nonlinear optical response[40] and high carrier mobility at room temperature.[40] These properties of Te are important for future applications.[41−44] Here, using scanning tunneling microscopy (STM), we report a surprising discovery of a stripe density modulation in Te. This powerful technique enables high spatial and energy resolutions in imaging Te single crystals along both cross-sectional and lateral orientations, revealing dramatic topographic and spectroscopic signatures.

Our investigation of Te single crystals begins with characterizing the crystal structure. The crystal's Bravais lattice exhibits a hexagonal symmetry, with lattice constants $a = b \simeq 4.5$ Å and $c \simeq 5.9$ Å. Within the (001) plane, the layers of Te atoms form a hexagonal lattice (Figure 1a, left panel). To visualize the atomic arrangement in the *ab* plane directly, we employ scanning transmission electron microscopy (STEM). This examination reveals a pristine, single-domain, hexagonal lattice structure (Figure 1b, left panel). Examining the $(1\bar{2}0)$ plane, we observe one-dimensional spiral chains of Te atoms, which are twisted along the *c* axis, giving rise to a distinct structural chirality (the crystal structure is displayed in the right panel of Figure 1a, with the corresponding STEM image in Figure 1b, right panel). This chirality manifest in two distinctive configurations, distinguished as right-handed and left-handed (associated with space groups $P3_121$ and $P3_221$, respectively). Using STEM, we confirmed that our Te sample consists of a single chiral domain, as depicted in Figure 1b.

Received: March 18, 2025
Revised: June 2, 2025
Accepted: June 4, 2025
Published: June 17, 2025

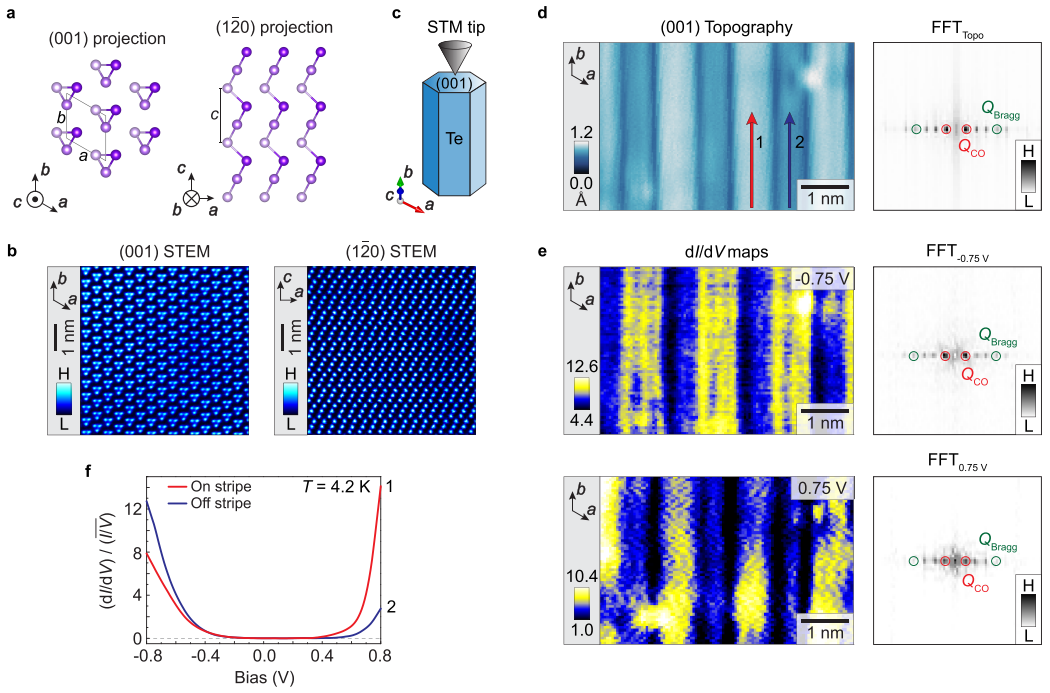

Figure 1. Stripe order in tellurium imaged through cross-sectional cleavage. (a) (001) and (1$\bar{2}$0) plane projections of the Te crystal structure. Te atoms located at different heights along the *c* axis are color-coded in the schematic. The (001) plane exhibits a hexagonal lattice, while the (1$\bar{2}$0) plane projection displays spiral atomic chains. Primitive unit cell vectors ($a = b \simeq 4.5$ Å, $c \simeq 5.9$ Å) are marked. (b) STEM images of (001) and (1$\bar{2}$0) crystallographic planes, showing a single chiral domain of the crystal. (c) Sketch of the cross-sectional sample cleavage geometry exposing the *ab* plane of the crystal. Here, the plane (001) is not a natural cleavage plane of the Te crystal due to the breakdown of strong covalent atomic bonds along spiral atomic chains. (d) Topographic image taken on the *ab* plane and the corresponding Fourier transform showing a spatially periodic modulation associated with a stripe order ($V_{gap} = -0.8$ V; $I_t = 50$ pA). The Fourier transform highlights the stripe order (red circles) and Bragg peaks (green circles), with other peaks being multiples of Q_{CO}. The stripe order period is $\lambda_{CO} \simeq 15.5$ Å ($\simeq 4$ atomic layers along the *ac* plane) determined from the position of the stripe order wavevector peak, signaling a 4 × 1 order. (e) dI/dV maps taken at −0.75 V (top panel) and 0.75 V (bottom panel), with the corresponding topography shown in panel d. dI/dV maps (left panels) and the accompanying Fourier transforms (right panels) reveal periodic charge modulation. The locations of the stripe order wavevector peaks (red circles) match those in the Fourier transform of the topography. The local density of states maxima (minima) at −0.75 V correspond to the local density of states minima (maxima) at 0.75 V. Tunneling junction setup: $V_{set} = -0.8$ V, $I_{set} = 0.3$ nA, and $V_{mod} = 10$ mV. (f) Color-coded spatially averaged normalized $(dI/dV)/(\overline{I/V})$ spectra acquired on and off the stripe, with their respective locations marked by the corresponding color-coded lines in the topographic image in panel d. The tunneling spectra on and off the stripe exhibit different spectroscopic gaps: $\Delta_{On} \simeq 400$ meV and $\Delta_{Off} \simeq 510$ meV. Tunneling junction setup: $V_{set} = -0.8$ V, $I_{set} = 0.3$ nA, and $V_{mod} = 5$ mV.

Although the neighboring atomic chains are only weakly bound by van der Waals forces, each Te atom forms strong covalent bonds with its two nearest neighbors within each chain.

To tunnel into the (001) plane, we performed a cross-sectional cleavage of the Te sample (Figure 1c) under ultrahigh-vacuum conditions (<5 × 10^{-10} mbar). Large-scale (001) topography images reveal highly corrugated surface areas, with a few flat regions of about 5 × 5 nm^2 on average (Figure S1). Topographic imaging of such region on the (001) plane at $T = 4.2$ K reveals a striking, periodic, striped modulation (Figure 1d), which is consistent with the presence of a charge modulation.[45,46] By identifying the Bragg and superlattice peaks in the Fourier transform image of the topography, we determine that the superlattice period is $\lambda \simeq 15.5$ Å, indicating a 4 × 1, unidirectional superstructure that breaks the lattice translational symmetry of the *ab* plane. Further details on the identification process of the Bragg and superlattice peaks can be found in Figure S2.

Spectroscopic imaging on the occupied (−0.75 V) and unoccupied (0.75 V) sides of the energy gap also reveals a 4 × 1-striped modulation, accompanied by a reversal of the spectroscopic contrast upon switching bias. Specifically, the local density of states maxima (minima) on the occupied side correspond to the local density of states minima (maxima) on the unoccupied side (Figure 1e), consistent with the electronic nature of the striped modulation.[46−48] Moreover, we find that the wavevector peaks of the charge modulation, as obtained from the Fourier transforms of the dI/dV maps, coincide with those of the superlattice in the Fourier transform of the topography. This observation suggests that the striped modulation in the topography originates from the charge modulation. Therefore, the striped charge modulation revealed by the topography and dI/dV maps suggest a stripe charge order.[14,45,49]

Upon visualizing the stripe order, we performed energy-resolved tunneling measurements. The spatially averaged normalized dI/dV spectra acquired on and off the stripe (as identified by the topographic images) exhibit differing spectroscopic energy gaps: $\Delta_{On} \simeq 400$ meV (Figure 1f, red curve) and $\Delta_{Off} \simeq 510$ meV (Figure 1f, blue curve). We refer to the Supporting Information and Figure S3 for more details on the extraction of the energy gap and the normalization procedure of dI/dV spectra. It is worth noting that these energy gap values appear to be somewhat larger than those observed in optical measurements.[50] This discrepancy may be

https://doi.org/10.1021/acs.nanolett.5c01695
Nano Lett. XXXX, XXX, XXX−XXX

attributed to tip-induced band-bending effects, which can potentially lead to an overestimation of the spectral gap size (as acquired from tunneling spectroscopy) in insulators or semiconductors.[51] Of particular importance is that the dI/dV spectra acquired on and off the stripe display an energy gap difference of $\Delta_{Off} - \Delta_{On} \simeq 110$ meV at 4.2 K, indicating an energy-gap modulation associated with the stripe order.

To explore whether the observed stripe order arises from spontaneous symmetry breaking, we conducted temperature-dependent tunneling measurements. In Figure 2a, we present

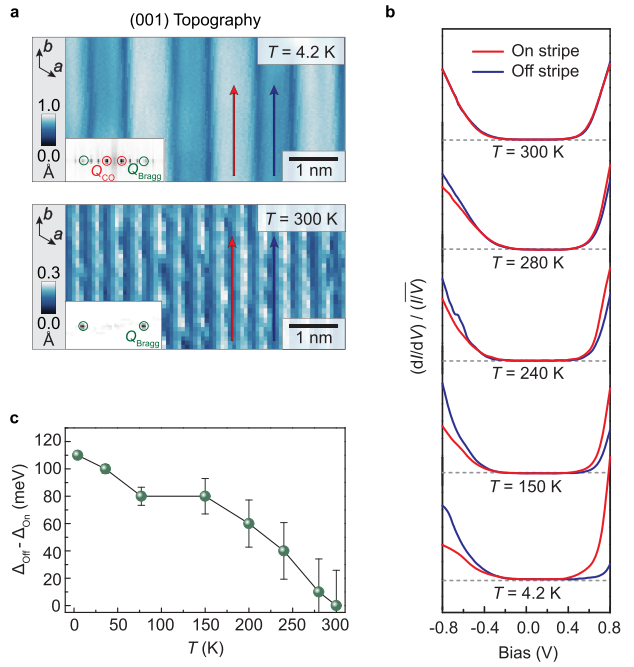

Figure 2. Temperature evolution of the stripe order. (a) Cross-sectional (*ab* plane) topographic images of the Te crystal at two different temperatures, with insets displaying the corresponding Fourier transforms. At T = 4.2 K, the data reveal charge-order peaks (red circles in the Fourier transform image), while no charge order is visible at T = 300 K. (b) Temperature dependence of spatially averaged normalized $(dI/dV)/(\overline{I/V})$ spectra acquired at on (red curves) and off (blue curves) the stripe regions. The spectra are spatially averaged along the corresponding color-coded lines marked in the topographic image (top of panel a). Spectra at different temperatures are vertically offset for clarity. Gray dashed lines denote dI/dV = 0 for each set of spectra. dI/dV spectroscopy tunneling junction setup: $V_{set} = -0.8$ V, $I_{set} = 0.3$ nA, and $V_{mod} = 5$ mV. (c) Energy gap difference between the on-stripe (Δ_{On}) and off-stripe (Δ_{Off}) regions plotted against temperature. The thermal broadening energy for each data point is indicated using the vertical bars. The energy gap difference decreases with increasing temperature and approaches zero at approximately T = 300 K.

topographic images of the (001) cleavage plane and their Fourier transforms acquired at two temperatures: T = 4.2 and 300 K. While the stripe order is prominent at T = 4.2 K, there is no discernible sign of stripe order at T = 300 K. We note that our topographic imaging of Te (001) does not provide clear resolution of individual atoms. Nevertheless, through analysis of the Fourier transforms, we identified the Bragg and superlattice peaks, indicated in the insets of Figure 2a (we refer the reader to Supporting Information and Figure S2 for detailed explanations). To illustrate the temperature dependence, Figure 2b showcases spatially averaged normalized dI/dV curves collected at on- and off-stripe regions across temperatures ranging from 4.2 to 300 K. Notably, as the temperature increases, the spectroscopic dissimilarity between the dI/dV curves of on- and off-stripe regions diminishes significantly. While there is a distinguishable difference between the curves at T = 280 K, they become similar at T = 300 K, as evidenced by the on- and off-stripe dI/dV ratio at ± 0.75 V (Figure S4). Interestingly, despite the weak spectroscopic dissimilarity of the curves at T = 280 K, this difference does not manifest in the topography (likely due to the weak modulation strength of the stripe order at 280 K), where the superlattice peaks are not discernible (Figure S2). Quantitatively, the energy gap difference $\Delta_{Off} - \Delta_{On}$ decreases nonlinearly with rising temperature, ultimately falling below the thermal broadening energy at T = 280 K and reaching zero at T = 300 K (Figure 2c). This decrease of the energy gap difference is accompanied by the vanishing of the spectroscopic dissimilarity of the dI/dV curves (Figure S4). These findings suggest that the onset temperature of the energy gap modulation and the associated stripe order is around room temperature, aligning with the topographic observations (Figure 2a). Taken together, the temperature-dependent tunneling data (Figure 2) provide an estimate of the charge-order onset temperature, $T_{CO} = 290 \pm 10$ K.

Building on our cross-sectional STM findings, we focus on the natural cleavage plane, (100) (Figure 3a). The bottom panel of Figure 3a provides a view of the (100) cleavage plane with Te atoms color-coded based on their respective heights relative to the cleavage plane. All three atomic sublattices—top, middle, and bottom—individually form a rectangular lattice. However, it is noteworthy that STM topographic measurements routinely resolve only the topmost atoms (see Figure S5 for bias-dependent atomic resolution). It is worth emphasizing that when viewed from the (100) plane, the 4 × 1 stripe charge order, which appears along the (001) plane, should manifest as an interlayer charge modulation with a 4-atomic layer periodicity. To visualize this interlayer charge ordering, we explore adjacent atomic layers separated by naturally occurring atomic step edges. This method enables us to capture images of multiple atomic layers parallel to this cleavage plane.

Here, we present two representative examples. Figure 3b (left panel) displays the topography of a defect-free bilayer step edge, along with a topographic linecut taken perpendicular to the edge's direction. On both sides of the edge, the terraces exhibit a uniform atomic correlation, as evidenced by the topographic linecut in the corresponding bottom panel. To determine the number of layers within the step edge, we analyze the height difference between two atomically flat terraces separated by the edge. Once we identify a bilayer step edge, we preform tunneling spectroscopy measurements on the two adjacent atomic layers (Figure 3b). The dI/dV map at −0.75 V reveals a pronounced spectroscopic contrast in the average dI/dV signal between the adjacent terraces, a contrast much greater than the atomic variation of dI/dV within a single terrace (Figure 3b). Moreover, the dI/dV maps display a switch in the spectroscopic contrast, with the terrace exhibiting high (low) dI/dV at −0.75 V now showing low (high) dI/dV at 0.75 V. By comparing the dI/dV map data (including the sign of contrast) with the cross-sectional dI/dV map data at −0.75 and +0.75 V presented in Figure 1, we can identify the on- and off-stripe regions. For instance, the on-stripe region

https://doi.org/10.1021/acs.nanolett.5c01695
Nano Lett. XXXX, XXX, XXX−XXX

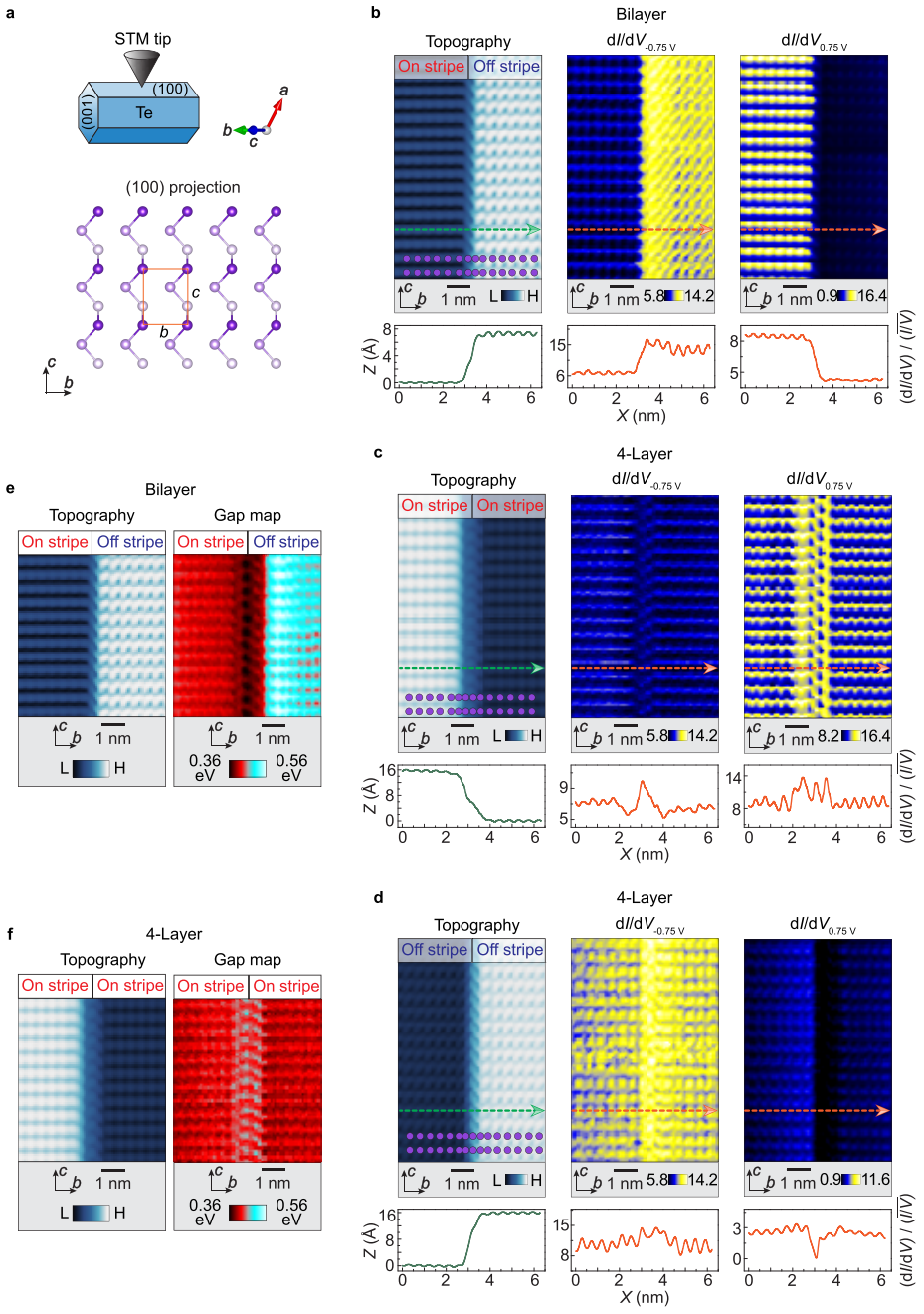

Figure 3. Spectroscopic mapping of adjacent atomic layers of Te (through natural lateral cleavage). (a) Top: Schematic of the lateral sample cleavage geometry exposing the (100) plane of the crystal. The (100) plane is a natural cleavage plane of Te due to the weak van der Waals bonding of adjacent atomic spiral chains. Bottom: Schematic depiction of the (100) plane projection of the crystal structure. Te atoms located at different heights with respect to the (100) plane are color-coded in the schematic. Individually equal-height atomic sublattices form a rectangular lattice with b and c lattice constants. Orange rectangle marks the surface primitive unit cell. (b) Topographic image and corresponding dI/dV maps taken at −0.75 and +0.75 V, showing a reversal of spectroscopic contrast between adjacent terraces separated by a bilayer step edge. Bottom of the topographic image: Height profile along the green dashed line, perpendicular to the c axis. Bottom panel of dI/dV maps: dI/dV linecuts along orange dashed lines in the maps. (c) Topographic image and corresponding dI/dV maps taken at −0.75 and +0.75 V, indicating no spectroscopic contrast between two on-stripe atomic layers separated by a four-layer step edge. (d) Topographic image and corresponding dI/dV maps taken at −0.75 and +0.75 V, showing no spectroscopic contrast between two off-stripe atomic layers separated by a four-layer step edge. The bottom panels of the topographic images display height profiles along green dashed lines, perpendicular to the c axis, while the bottom panels of dI/dV maps show dI/dV linecuts along orange dashed lines in the corresponding maps. Schematics of the Te top atom positions, based on its crystallographic structure, are overlaid on the topographic images in panels b–d, with Te atoms represented as dark-purple circles. Tunneling junction setup for dI/dV maps: V_{set} = −0.8 V, I_{set} = 0.3 nA, and V_{mod} = 10 mV. (e) Left: Topographic image of adjacent atomic layers separated by a bilayer step edge (V_{gap} = −0.8 V; I_t = 100 pA). Right: Corresponding spectroscopic gap map, revealing a difference of $\Delta_{Off} - \Delta_{On} \simeq 110$ meV in average gap magnitude between on-stripe and off-stripe atomic layers. (f) Left: Topographic image of two adjacent atomic layers separated by a four-layer step edge (V_{gap} = −0.8 V; I_t = 100 pA). Right: Corresponding spectroscopic gap map, showing no discernible difference in the gap magnitude between both on-stripe atomic layers. All data are collected at 4.2 K.

https://doi.org/10.1021/acs.nanolett.5c01695
Nano Lett. XXXX, XXX, XXX−XXX

exhibits higher dI/dV at 0.75 V and lower dI/dV at −0.75 V compared to the off-stripe region.

Having observed the spectroscopic contrast and its switch between the adjacent terraces separated by a bilayer step edge, we turn our attention to our second example, which involves a four-layer atomic step edge as identified in the topographic image in Figure 3c. Contrary to the case with terraces separated by a bilayer step edge (Figure 3b), spectroscopic imaging at −0.75 and +0.75 V reveals no discernible contrast between the two adjacent terraces in Figure 3c, which are separated by a four-layer step edge. As previously described, based on the spectroscopic contrast, both terraces in Figure 3c represent on-stripe regions. Additionally, we identified two off-stripe terraces separated by a four-layer step edge, as depicted in Figure 3d. As expected, due to the 4-atomic-layer periodicity, no spectroscopic difference between the two off-stripe terraces is detected (Figure 3d). Overall, the dI/dV maps at −0.75 and +0.75 V reveal a spectroscopic contrast between the terraces separated by a bilayer step edge, while showing no spectroscopic difference between the terraces separated by a four-layer step edge. Our extended investigation of the various terraces on the Te (100) surface reveals the presence of four distinct types of spectra, each corresponding to a unique terrace (Figure S6). Notably, these spectra can be grouped into two pairs, with each pair exhibiting qualitatively similar features. However, clear spectroscopic contrast between the two pairs is observed at bias voltages of −0.75 and +0.75 V Taken together, these observations align with the presence of a 4 × 1 stripe charge order along the (001) plane, which now, when probed along the (100) plane, manifests as an interlayer charge modulation with a 4-atomic-layer periodicity.

Notably, we examined the temperature dependence of the spectroscopic contrast observed in adjacent terraces separated by the bilayer step edge (Figure S7). We find that the spectroscopic contrast becomes quite suppressed at T = 280 K. This observation aligns with the temperature-dependent spectroscopic results presented in Figure 2, where the stripe order is probed on the (001) plane. Collectively, the observation of a consistent charge order from two different crystallographic planes provides compelling evidence for the bulk nature of the stripe charge order.

Next, we extract the energy gap value from every dI/dV spectrum of the dI/dV map and plot a spatial distribution of the energy gap, also known as a gap map.[52] Panels e and f of Figure 3 depict the gap maps for two adjacent terraces separated by bilayer and four-layer step edges, respectively. In both cases, the energy gap within each layer shows atomic correlations. However, the average gap magnitudes on the two terraces separated by a bilayer step edge differ (Figure 3e). This gap difference (between on- and off-stripe regions) is consistent with the data for Te (001) presented in Figures 1 and 2. Continuing the analysis of the gap difference between terraces, the two terraces (of on-stripe region) separated by a four-layer step edge show no detectable gap difference (Figure 3f). It is worth noting that we do detect an increase in energy gap at the slope of the four-layer edge. Due to the crystal geometry, multilayer step edges in Te appear to be slanted, and a tunneling tip probes protruding edge parts of the atomic layers located between the top and bottom terraces. This gap increase at the slope of the four-layer edge indicates that the off-stripe atomic layers are sandwiched among the on-stripe atomic layers. We emphasize that while the magnitude of the dI/dV spectra is influenced by both the tip and the sample, the energy gap typically correlates primarily with the electronic nature of the sample. Therefore, the spatial gap modulation associated with the charge order—observed in several charge density wave compounds—has been interpreted as evidence for the electronic nature of the charge order.[46,48] Similarly, our observation of the gap modulation associated with the stripe order strongly suggests its electronic nature. We note that our observation of stripe charge modulation—evident through dI/dV maps, energy gap maps, and the temperature dependence of gap modulation—differs from what is expected from surface reconstruction effects (e.g., as seen on the surfaces of Au and Si[53,54]). Instead, it represents a stripe charge order observed for the first time in a topological elemental solid.

To provide further evidence for the charge order's bulk nature we employ X-ray scattering. In Figure 4a, we present the reciprocal space representation of the 4 × 1 stripe order as probed in our tunneling experiments. To capture this stripe order in our X-ray scattering experiments, we conducted several scans illustrated in Figure 4c (see the reciprocal space representation of the stripe order observed in X-ray scattering in Figure 4b). The X-ray scattering measurements reveal superlattice peaks at H = 1.5 and 1.73, which upon translation to the first Brillouin zone coincide with the stripe order peaks obtained from the tunneling experiments. We note that the absence of superlattice peak at (1.5, 0, 0) can be attributed to the diffraction selection rules. Upon closer examination, the superlattice peaks have Lorentzian shape with the full width of 0.016 r.l.u. at half-maximum, suggesting ∼10 nm domain size. Notably, the superlattice peak intensity is approximately 10^3–10^4 times weaker than their neighboring fundamental Bragg peaks. Such a low intensity of the superlattice peak is consistent with the charge order, which induces small lattice distortion. Moreover, this dramatic disparity between the superlattice and Bragg peak strengths provides an upper-bound estimate for potential lattice displacements, which is remarkably small, measuring at $\lesssim 10^{-2}$ Å.

Concomitantly, changes to the electronic structure imposed by charge ordering could also impact the transport properties of Te. Upon closer inspection of tunneling spectra (Figure 2b), a valence band edge can be seen to shift between on- and off-stripe regions (Figure S8). The emergent unidirectional periodicity of the hole potential would imply the splitting of the valence bands, potentially affecting the transverse effective mass of holes, whereas domain boundaries can act as an additional scattering mechanism. Remarkably, magnetotransport studies of clean bulk Te crystals indeed reveal several anomalies in the vicinity of the charge-ordering temperature, T_{CO} = 290 ± 10 K. Interchain hole mobility exhibits a kink around 290 K, while the intrachain one remains featureless.[55] Most surprisingly, the lower Hall sign reversal temperature—the hallmark piece of the Te puzzle[56,57]—converges toward T_{CO} as a function of the magnetic field for both inter- and intrachain directions.[58] These observations are consistent with the bulk stripe order reported here, making this previously overlooked ordering the missing piece necessary to reconcile the long-debated nature of the charge transport in Te.

Potential interchain structural instability was noted early on and recently has come into the spotlight in studies of the 2D Te variant, tellurene, due in part to its inclination toward structural reconstructions.[59−67] STM investigations on multilayered tellurene indeed revealed the theoretically predicted β-Te phase, characterized by a shrunk rectangular unit cell and an enlarged energy gap.[62] Interestingly, these studies observed

https://doi.org/10.1021/acs.nanolett.5c01695
Nano Lett. XXXX, XXX, XXX−XXX

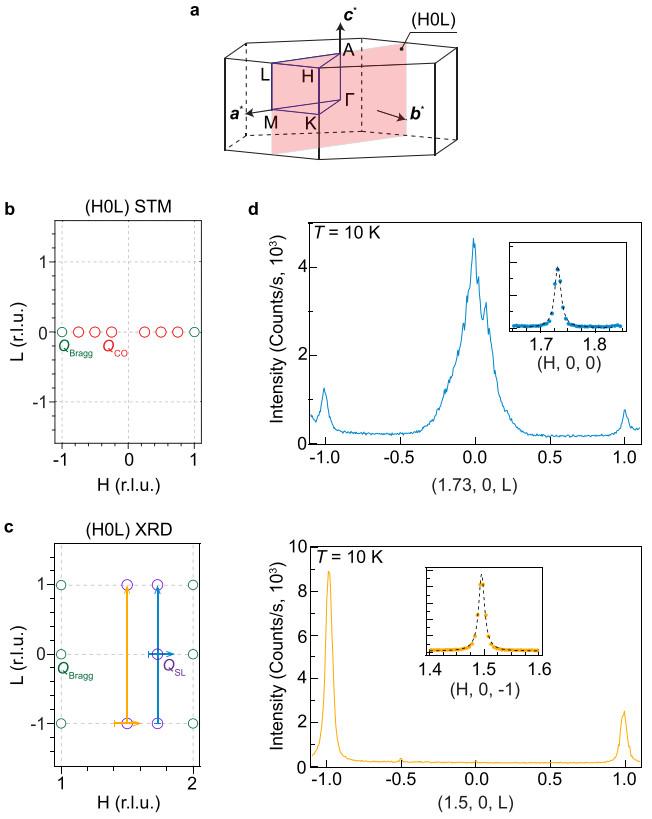

Figure 4. X-ray diffraction signatures of the stripe order. (a) Schematics of the first Brillouin zone of Te. a^*, b^*, and c^* denote reciprocal lattice vectors; H, K, and L are the corresponding reciprocal space coordinates. High symmetry points of the first Brillouin zone are marked with the capital Greek letters. The $(H0L)$ reciprocal space plane, which was probed in STM and X-ray diffraction experiments (panels b and c), is marked with a red rectangle. (b) Reciprocal space representation of the charge order in the $(H0L)$ plane observed in STM measurements. Stripe order (Bragg) peaks are marked with red (green) circles. (c) Reciprocal space representation of the stripe order in the $(H0L)$ plane observed in X-ray scattering. Superlattice (Bragg) peaks are marked with purple (green) circles. Upon translation to the first Brillouin zone superlattice peaks at $H = 1.5$ and 1.73 acquire the same H coordinate as the stripe order peaks from tunneling measurements in panel b. (d) Top: X-ray scattering scan at $T = 10$ K along the $(1.73, 0, L)$ direction in the reciprocal space. The inset shows H scan along the $(H, 0, 0)$ direction. Bottom: X-ray scattering scan along the $(1.5, 0, L)$ direction. Inset illustrates H scan along the $(H, 0, -1)$ direction. The locations of X-ray scattering scans in the reciprocal space are also marked with the corresponding color-coded arrowhead lines in panel c; the direction of the X-ray scan is marked with an arrow. The superlattices at $(1.73, 0, 0)$ and $(1.5, 0, -1)$ are consistent with the $4a$ superstructure observed in STM measurements. Dashed curves represent the Lorentzian function fit of the superlattice peaks. The extracted full width at half-maxima are 0.016 in reciprocal lattice units for both the $H = 1.5$ and 1.73 peaks. The superlattice peak intensity is about 10^3–10^4 times weaker than their nearby fundamental Bragg peaks, providing an upper-bound estimate on lattice displacements of $\lesssim 10^{-2}$ Å.

a monotonic decrease in the energy gap as the number of Te layers increased, yet no periodic interlayer modulation of tellurene was reported.[62,63] Thus, the existence of a critical thickness necessary for the stability of the 4-layer periodic modulation demonstrated in this study emphasizes the competing structural orders. Fluctuating stripe order could still affect the transport properties in 2D crystals, calling for further investigation.

Before concluding, we note that charge order in some materials has been attributed to a Peierls instability driven by Fermi surface nesting and the resulting divergence in electronic susceptibility.[68−70] However, in Te, the Fermi level lies within the bandgap, precluding the existence of a Fermi surface necessary for such a mechanism. This makes the classical Peierls scenario unlikely. Understanding the origin of this charge order will require future theoretical efforts.

In summary, our comprehensive tunneling measurements on two different crystallographic planes, along with X-ray diffraction data, reveal a 4 × 1 stripe order in Te, which breaks the translational symmetry of the crystal. Notably, the stripe order has been overlooked despite Te being under study for over 70 years.[71−73] Identification of the superstructure in early X-ray diffraction studies remained elusive.[74] This challenge can be attributed to the extremely weak intensity of the superlattice peaks, necessitating high-resolution low-temperature measurements using hard X-rays that we employed for their detection and ultimately, the insight into the superstructure periodicity from tunneling spectra. It is surprising that such an electronic stripe phase, which is typically observed in strongly correlated systems, apparently also appears in a weakly correlated system (Te). This observation also marks the first identification of a stripe order within a topological elemental solid. Notably, its onset temperature resides very close to room temperature, making it particularly attractive for practical applications. Our observation of a stripe phase in a tunable semiconducting topological material will provide a versatile experimental platform for exploring the interplay between charge order, chirality, and topology.

■ ASSOCIATED CONTENT

Data Availability Statement

All data needed to evaluate the conclusions in the paper are present in the paper. Additional data are available from the corresponding authors upon request.

Supporting Information

The Supporting Information is available free of charge at https://pubs.acs.org/doi/10.1021/acs.nanolett.5c01695.

Te single-crystal growth, details of experimental methods, normalization of dI/dV spectra, large-scale Te (001) topographic images, identification of Bragg peaks in the Fourier transform of Te (001) topography, energy gap determination from tunneling spectra, different types of tunneling spectra identified on Te (100) terraces, temperature dependence of the spectroscopic contrast between on-stripe and off-stripe Te (100) atomic layers, and selected-area electron diffraction measurements (PDF)

■ AUTHOR INFORMATION

Corresponding Authors

Md Shafayat Hossain − *Laboratory for Topological Quantum Matter and Advanced Spectroscopy (B7), Department of Physics, Princeton University, Princeton, New Jersey 08540, United States;* orcid.org/0000-0002-3744-5877; Email: mdsh@princeton.edu

M. Zahid Hasan − *Laboratory for Topological Quantum Matter and Advanced Spectroscopy (B7), Department of*

https://doi.org/10.1021/acs.nanolett.5c01695
Nano Lett. XXXX, XXX, XXX−XXX

Physics, Princeton University, Princeton, New Jersey 08540, United States; Email: mzhasan@princeton.edu

Authors

Maksim Litskevich − *Laboratory for Topological Quantum Matter and Advanced Spectroscopy (B7), Department of Physics, Princeton University, Princeton, New Jersey 08540, United States*

Yang Fu − *Department of Physics and Beijing Key Laboratory of Optoelectronic Functional Materials & MicroNano Devices, Renmin University of China, Beijing 100872, China; Key Laboratory of Quantum State Construction and Manipulation (Ministry of Education), Renmin University of China, Beijing 100872, China*

Hu Miao − *Materials Science and Technology Division, Oak Ridge National Laboratory, Oak Ridge, Tennessee 37831, United States*

Yuxiao Jiang − *Laboratory for Topological Quantum Matter and Advanced Spectroscopy (B7), Department of Physics, Princeton University, Princeton, New Jersey 08540, United States*

Guangming Cheng − *Princeton Institute for Science and Technology of Materials, Princeton University, Princeton, New Jersey 08544, United States*; orcid.org/0000-0001-5852-1341

Pengcheng Chen − *Princeton Institute for Science and Technology of Materials, Princeton University, Princeton, New Jersey 08544, United States*; orcid.org/0000-0003-2018-5594

Qi Zhang − *Laboratory for Topological Quantum Matter and Advanced Spectroscopy (B7), Department of Physics, Princeton University, Princeton, New Jersey 08540, United States*

Zi-Jia Cheng − *Laboratory for Topological Quantum Matter and Advanced Spectroscopy (B7), Department of Physics, Princeton University, Princeton, New Jersey 08540, United States*

Raul Acevedo-Esteves − *National Synchrotron Light Source II, Brookhaven National Laboratory, Upton, New York 11973, United States*; orcid.org/0000-0003-3668-7089

Christie Nelson − *National Synchrotron Light Source II, Brookhaven National Laboratory, Upton, New York 11973, United States*; orcid.org/0000-0002-0196-0340

Haozhe Wang − *Department of Chemistry, Michigan State University, East Lansing, Michigan 48824, United States*; orcid.org/0000-0003-4820-833X

Jose L. Gonzalez Jimenez − *Department of Chemistry, Michigan State University, East Lansing, Michigan 48824, United States*

Brian Casas − *National High Magnetic Field Laboratory, Florida State University, Tallahassee, Florida 32310, United States*

Xiaoxiong Liu − *Shenzhen Institute for Quantum Science and Engineering and Department of Physics, Southern University of Science and Technology, Shenzhen 518055, China*

Stepan S. Tsirkin − *Centro de Física de Materiales, Universidad del País Vasco, San Sebastián 20018, Spain; Ikerbasque Foundation, Bilbao 48013, Spain; Chair of Computational Condensed Matter Physics, Institute of Physics, École Polytechnique Fédérale de Lausanne (EPFL), CH-1015 Lausanne, Switzerland*

Kouta Dagnino − *Department of Physics, University of Zürich, Zürich 8057, Switzerland*

Songbo Zhang − *Department of Physics, University of Zürich, Zürich 8057, Switzerland*

Chia-Hsiu Hsu − *Division of Physics and Applied Physics, School of Physical and Mathematical Sciences, Nanyang Technological University, Singapore 637371, Singapore*

Sen Shao − *Division of Physics and Applied Physics, School of Physical and Mathematical Sciences, Nanyang Technological University, Singapore 637371, Singapore*

Shaogang Xu − *Department of Physics, Southern University of Science and Technology, Shenzhen 518055, China*

Tyler A. Cochran − *Laboratory for Topological Quantum Matter and Advanced Spectroscopy (B7), Department of Physics, Princeton University, Princeton, New Jersey 08540, United States*

Xian P. Yang − *Laboratory for Topological Quantum Matter and Advanced Spectroscopy (B7), Department of Physics, Princeton University, Princeton, New Jersey 08540, United States*

Hu Xu − *Department of Physics, Southern University of Science and Technology, Shenzhen 518055, China*; orcid.org/0000-0002-2254-5840

Jiaxin Yin − *Laboratory for Topological Quantum Matter and Advanced Spectroscopy (B7), Department of Physics, Princeton University, Princeton, New Jersey 08540, United States; Department of Physics, Southern University of Science and Technology, Shenzhen 518055, China*

Yaroslav A. Gerasimenko − *Department of Physics and Regensburg Center for Ultrafast Nanoscopy, University of Regensburg, Regensburg 93040, Germany*

Weiwei Xie − *Department of Chemistry, Michigan State University, East Lansing, Michigan 48824, United States*; orcid.org/0000-0002-5500-8195

Nan Yao − *Princeton Institute for Science and Technology of Materials, Princeton University, Princeton, New Jersey 08544, United States*; orcid.org/0000-0002-4081-1495

Luis Balicas − *National High Magnetic Field Laboratory and Department of Physics, Florida State University, Tallahassee, Florida 32310, United States*; orcid.org/0000-0002-5209-0293

Guoqing Chang − *Division of Physics and Applied Physics, School of Physical and Mathematical Sciences, Nanyang Technological University, Singapore 637371, Singapore*; orcid.org/0000-0003-1180-3127

Titus Neupert − *Department of Physics, University of Zürich, Zürich 8057, Switzerland*

Hechang Lei − *Department of Physics and Beijing Key Laboratory of Optoelectronic Functional Materials & MicroNano Devices, Renmin University of China, Beijing 100872, China; Key Laboratory of Quantum State Construction and Manipulation (Ministry of Education), Renmin University of China, Beijing 100872, China*

Complete contact information is available at: https://pubs.acs.org/10.1021/acs.nanolett.5c01695

Author Contributions

†M.L., M.S.H., and Y.F. contributed equally to this work.

Notes

The authors declare no competing financial interest.

■ ACKNOWLEDGMENTS

We are grateful to P. Padmanabhan for helpful discussions.M.Z.H.'s group at Princeton University acknowledges

https://doi.org/10.1021/acs.nanolett.5c01695
Nano Lett. XXXX, XXX, XXX−XXX

primary support from the US Department of Energy (DOE), Office of Science, under the Basic Energy Sciences (DOE-BES) programme (Grant No. DOE/BES DE-FG-02-05ER46200) for the advanced spectroscopic measurements and theoretical including ARPES and the National Quantum Information Science Research Centers, the Quantum Science Center and Princeton University; ARPES, STM and transport instrumentation support from the Gordon and Betty Moore Foundation (Grant No. GBMF9461)and Princeton University; and support from the US DOE under the Basic Energy Sciences (DOE-BES) programme (Grant No. DOE/BES DE-FG-02- 05ER46200) for the theoretical work and extensive sample characterization. J.L.G.J., H.W., and W.X. were supported by the Beckman Young Investigator award. H.L. acknowledges support from the National Key R&D Program of China (Grants 2023YFA1406500 and 2022YFA1403800) and National Natural Science Foundation of China (Grant 12274459). S.S.T. acknowledges funding by MCIN/AEI/10.13039/501100011033 through Grant PID2021-129035NB-I00 and the European Union (H2020-MSCA-COFUND-2020-101034228-WOLFRAM2). T.N. acknowledges support from the Swiss National Science Foundation through a Consolidator Grant (iTQC, TMCG-2_213805). L.B. is supported by DOE-BES through the award DE-SC0002613. The National High Magnetic Field Laboratory acknowledges support from the US-NSF Cooperative agreement Grant number DMR-DMR-2128556 and the state of Florida. The authors acknowledge the use of Princeton's Imaging and Analysis Center, which is partially supported by the Princeton Center for Complex Materials, a National Science Foundation (NSF)-MRSEC program (DMR-2011750). Y. G. has been supported by the Deutsche Forschungsgemeinschaft (DFG, German Research Foundation) through Project-ID 314695032—SFB 1277. Work at Nanyang Technological University was supported by the National Research Foundation, Singapore, under its Fellowship Award (NRF-NRFF13-2021-0010), the Singapore Ministry of Education (MOE) Academic Research Fund Tier 3 grant (MOE-MOET32023-0003), and the Nanyang Assistant Professorship grant (NTU-SUG).

REFERENCES

(1) Landau, L. On the theory of phase transitions. *Zh. Eksp. Teor. Fiz.* **1937**, *7*, 19−32.
(2) Grüner, G. The dynamics of charge-density waves. *Rev. Mod. Phys.* **1988**, *60*, 1129−1181.
(3) Grüner, G. *Density Waves in Solids*; Addison-Wesley, 1994.
(4) Kivelson, S.; Fradkin, E.; Emery, V. Electronic liquid-crystal phases of a doped Mott insulator. *Nature* **1998**, *393*, 550−553.
(5) Emery, V. J.; Kivelson, S. A.; Tranquada, J. M. Stripe phases in high-temperature superconductors. *Proc. Natl. Acad. Sci. U.S.A.* **1999**, *96*, 8814.
(6) Berthier, C., Levy, L.-P., Martinez, G., Eds. *High Magnetic Fields: Applications in Condensed Matter Physics and Spectroscopy*; Springer-Verlag: Berlin, 2002.
(7) Fradkin, E.; Kivelson, S. A.; Lawler, M. J.; Eisenstein, J. P.; Mackenzie, A. P. Nematic Fermi Fluids in Condensed Matter Physics. *Annu. Rev. Condens. Matter Phys.* **2010**, *1*, 153−178.
(8) Tranquada, J. M.; Sternlieb, B. J.; Axe, J. D.; Nakamura, Y.; Uchida, S. Evidence for stripe correlations of spins and holes in copper oxide superconductors. *Nature* **1995**, *375*, 561−563.
(9) Tranquada, J. M.; et al. Neutron-scattering study of stripe-phase order of holes and spins in $La_{1.48}Nd_{0.4}Sr_{0.12}CuO_4$. *Phys. Rev. B* **1996**, *54*, 7489−7499.
(10) Abbamonte, P.; Rusydi, A.; Smadici, S.; et al. Spatially modulated 'Mottness' in $La_{2-x}Ba_xCuO_4$. *Nat. Phys.* **2005**, *1*, 155−158.
(11) Comin, R.; et al. Broken translational and rotational symmetry via charge stripe order in underdoped $YBa_2Cu_3O_{6+y}$. *Science* **2015**, *347*, 1335−1339.
(12) Vojta, M. Lattice symmetry breaking in cuprate superconductors: stripes, nematics, and superconductivity. *Adv. Phys.* **2009**, *58*, 699−820.
(13) Fernandes, R.; Chubukov, A.; Schmalian, J. What drives nematic order in iron-based superconductors? *Nat. Phys.* **2014**, *10*, 97−104.
(14) Yim, C. M.; Trainer, C.; Aluru, R.; Chi, S.; Hardy, W. N.; Liang, R.; Bonn, D.; Wahl, P. Discovery of a strain-stabilized smectic electronic order in LiFeAs. *Nat. Commun.* **2018**, *9*, 2602.
(15) Zhao, H.; Blackwell, R.; Thinel, M.; et al. Smectic pair-density-wave order in $EuRbFe_4As_4$. *Nature* **2023**, *618*, 940−945.
(16) Qin, T.; et al. Real-Space Observation of Unidirectional Charge Density Wave and Complex Structural Modulation in the Pnictide Superconductor $Ba_{1-x}Sr_xNi_2As_2$. *Nano Lett.* **2023**, *23* (7), 2958−2963.
(17) Koulakov, A. A.; Fogler, M. M.; Shklovskii, B. I. Charge Density Wave in Two-Dimensional Electron Liquid in Weak Magnetic Field. *Phys. Rev. Lett.* **1996**, *76*, 499.
(18) Du, R. R.; et al. Strongly anisotropic transport in higher two-dimensional Landau levels. *Solid State Commun.* **1999**, *109*, 389−394.
(19) Lilly, M. P.; et al. Evidence for an Anisotropic State of Two-Dimensional Electrons in High Landau Levels. *Phys. Rev. Lett.* **1999**, *82*, 394.
(20) Jin, C.; Tao, Z.; Li, T.; et al. Stripe phases in WSe_2/WS_2 moiré superlattices. *Nat. Mater.* **2021**, *20*, 940−944.
(21) Polshyn, H.; Zhang, Y.; Kumar, M. A.; et al. Topological charge density waves at half-integer filling of a moiré superlattice. *Nat. Phys.* **2022**, *18*, 42−47.
(22) Hasan, M. Z.; Chang, G.; Belopolski, I.; et al. Weyl, Dirac and high-fold chiral fermions in topological quantum matter. *Nat. Rev. Mater.* **2021**, *6*, 784−803.
(23) Chang, G.; Wieder, B. J.; Schindler, F.; et al. Topological quantum properties of chiral crystals. *Nat. Mater.* **2018**, *17*, 978−985.
(24) Jia, S.; Xu, S.-Y.; Hasan, M. Weyl semimetals, Fermi arcs and chiral anomalies. *Nat. Mater.* **2016**, *15*, 1140−1144.
(25) Hirayama, M.; et al. Weyl Node and Spin Texture in Trigonal Tellurium and Selenium. *Phys. Rev. Lett.* **2015**, *114*, 206401.
(26) Tsirkin, S. S.; Puente, P. A.; Souza, I. Gyrotropic effects in trigonal tellurium studied from first principles. *Phys. Rev. B* **2018**, *97*, No. 035158.
(27) Tsirkin, S. S.; Souza, I.; Vanderbilt, D. Composite Weyl nodes stabilized by screw symmetry with and without time-reversal invariance. *Phys. Rev. B* **2017**, *96*, No. 045102.
(28) Nakayama, K.; Kuno, M.; Yamauchi, K.; Souma, S.; Sugawara, K.; Oguchi, T.; Sato, T.; Takahashi, T.; et al. Band splitting and Weyl nodes in trigonal tellurium studied by angle-resolved photoemission spectroscopy and density functional theory. *Phys. Rev. B* **2017**, *95*, No. 125204.
(29) Zhang, N.; et al. Magnetotransport signatures of Weyl physics and discrete scale invariance in the elemental semiconductor tellurium. *Proc. Natl. Acad. Sci. USA* **2020**, *117*, 11337−11343.
(30) Qiu, G.; Niu, C.; Wang, Y.; et al. Quantum Hall effect of Weyl fermions in n-type semiconducting tellurene. *Nat. Nanotechnol.* **2020**, *15*, 585−591.
(31) Ma, J.; Cheng, B.; Li, L.; Fan, Z.; Mu, H.; Lai, J.; Song, X.; Yang, D.; Cheng, J.; Wang, Z.; Zeng, C.; Sun, D. Unveiling Weyl-related optical responses in semiconducting tellurium by mid-infrared circular photogalvanic effect. *Nat. Commun.* **2022**, *13*, 5425.
(32) Gatti, G.; et al. Radial Spin Texture of the Weyl Fermions in Chiral Tellurium. *Phys. Rev. Lett.* **2020**, *125*, 216402.
(33) Sakano, M.; et al. Radial Spin Texture in Elemental Tellurium with Chiral Crystal Structure. *Phys. Rev. Lett.* **2020**, *124*, 136404.
(34) Shi, Z.; Cao, R.; Khan, K.; Tareen, A. K.; Liu, X.; Liang, W.; Zhang, Y.; Ma, C.; Guo, Z.; Luo, X.; Zhang, H. Two-Dimensional Tellurium: Progress, Challenges, and Prospects. *Nano-Micro Lett.* **2020**, *12*, 99.

https://doi.org/10.1021/acs.nanolett.5c01695
Nano Lett. XXXX, XXX, XXX−XXX

(35) Peng, H.; Kioussis, N.; Snyder, G. J. Elemental tellurium as a chiral p-type thermoelectric material. *Phys. Rev. B* **2014**, *89*, No. 195206.
(36) Lin, S.; Li, W.; Chen, Z.; Shen, J.; Ge, B.; Pei, Y. Tellurium as a high-performance elemental thermoelectric. *Nat. Commun.* **2016**, *7*, 10287.
(37) Royer, D.; Dieulesaint, E. Elastic and piezoelectric constants of trigonal selenium and tellurium crystals. *J. Appl. Phys.* **1979**, *50*, 4042−4045.
(38) Arlt, G.; Quadflieg, P. Electronic displacement in tellurium by mechanical strain. *Phys. Status Solidi (b)* **1969**, *32*, 687−689.
(39) Pan, Y.; et al. Dependence of excited-state properties of tellurium on dimensionality: From bulk to two dimensions to one dimension. *Phys. Rev. B* **2018**, *98*, No. 085135.
(40) Wang, Y.; Qiu, G.; Wang, R.; et al. Field-effect transistors made from solution-grown two-dimensional tellurene. *Nat. Electron.* **2018**, *1*, 228−236.
(41) Qiu, G.; Charnas, A.; Niu, C.; Wang, Y.; Wu, W.; Ye, P. D. The resurrection of tellurium as an elemental two-dimensional semiconductor. *npj 2D Mater. Appl.* **2022**, *6*, 17.
(42) Chen, J.; Zhang, T.; Wang, J.; Xu, L.; Lin, Z.; Liu, J.; Wang, C.; Zhang, N.; Lau, S. P.; Zhang, W.; Chhowalla, M.; Chai, Y. Topological phase change transistors based on tellurium Weyl semiconductor. *Sci. Adv.* **2022**, *8*, 23.
(43) Hirobe, D.; Nabei, Y.; Yamamoto, H. M. Chirality-induced intrinsic charge rectification in a tellurium-based field-effect transistor. *Phys. Rev. B* **2022**, *106*, No. L220403.
(44) Rao, G.; Fang, H.; Zhou, T.; Zhao, C.; Shang, N.; Huang, J.; Liu, Y.; Du, X.; Li, P.; Jian, X.; Ma, L.; Wang, J.; Liu, K.; Wu, J.; Wang, X.; Xiong, J. Robust Piezoelectricity with Spontaneous Polarization in Monolayer Tellurene and Multilayer Tellurium Film at Room Temperature for Reliable Memory. *Adv. Mater.* **2022**, *34*, 35.
(45) Soumyanarayanan, A.; et al. Quantum phase transition from triangular to stripe charge order in $NbSe_2$. *Proc. Natl. Acad. Sci. U.S.A.* **2013**, *110*, 1623−1627.
(46) Li, G.; Yang, H.; Jiang, P.; Wang, C.; Cheng, Q.; Tian, S.; Han, G.; Shen, C.; Lin, X.; Lei, H.; Ji, W.; Wang, Z.; Gao, H.-J. Chirality locking charge density waves in a chiral crystal. *Nat. Commun.* **2022**, *13*, 2914.
(47) da Silva Neto, E. H.; Aynajian, P.; Baumbach, R. E.; Bauer, E. D.; Mydosh, J.; Ono, S.; Yazdani, A. Detection of electronic nematicity using scanning tunneling microscopy. *Phys. Rev. B* **2013**, *87*, 161117.
(48) Wang, Z.; et al. Electronic nature of chiral charge order in the kagome superconductor CsV_3Sb_5. *Phys. Rev. B* **2021**, *104*, 075148.
(49) Park, S.; Kim, S. Y.; Kim, H. K.; Kim, M. J.; Kim, T.; Kim, H.; Choi, G. S.; Won, C. J.; Kim, S.; Kim, K.; Talantsev, E. F.; Watanabe, K.; Taniguchi, T.; Cheong, S.-W.; Kim, B. J.; Yeom, H. W.; Kim, J.; Kim, T.-H.; Kim, J. S. Superconductivity emerging from a stripe charge order in $IrTe_2$ nanoflakes. *Nat. Commun.* **2021**, *12*, 3157.
(50) Anzin, V. B.; et al. Measurement of the energy gap in tellurium under pressure. *Phys. Status Solidi A* **1977**, *42*, 385.
(51) Butler, C. J.; Yoshida, M.; Hanaguri, T.; Iwasa, Y. Mottness versus unit-cell doubling as the driver of the insulating state in 1T-TaS_2. *Nat. Commun.* **2020**, *11*, 2477.
(52) Lee.; et al. Imaging Dirac-mass disorder from magnetic dopant atoms in the ferromagnetic topological insulator $Cr_x(Bi_{0.1}Sb_{0.9})_{2-x}Te_3$. *Proc. Natl. Acad. Sci. U.S.A.* **2015**, *112*, 1316−1321.
(53) Barth, V.; et al. Scanning tunneling microscopy observations on the reconstructed Au(111) surface: Atomic structure, long-range superstructure, rotational domains, and surface defects. *Phys. Rev. B* **1990**, *42*, 9307.
(54) Binnig, G.; et al. 7 × 7 Reconstruction on Si(111) Resolved in Real Space. *Phys. Rev. Lett.* **1983**, *50*, 120.
(55) Geick, R.; Grosse, P.; Richter, W. The contribution of the lattice vibrations to the optical constants of tellurium. In *The Physics of Selenium and Tellurium*; Cooper, W. Ch., Ed.; Pergamon, 1969; pp 309−318.
(56) Bottom, V. E. The Hall Effect and Electrical Resistivity of Tellurium. *Science* **1952**, *115*, 570−571.
(57) Nussbaum, A. Electrical Properties of Pure Tellurium and Tellurium-Selenium Alloys. *Phys. Rev.* **1954**, *94*, 337.
(58) Zimmermann, W. Galvanomagnetic Effects in Tellurium in Magnetic Fields up to 160 kG at Temperatures between 150 and 350 K. *Phys. Status Solidi (b)* **1970**, *37*, 619.
(59) Zhu, Z.; Cai, X.; Yi, S.; et al. Multivalency-Driven Formation of Te-Based Monolayer Materials: A Combined First-Principles and Experimental study. *Phys. Rev. Lett.* **2017**, *119*, 106101.
(60) Qiao, Y.; Pan, F.; Yang.; et al. Few-layer tellurium: one-dimensional-like layered elementary semi-conductor with striking physical properties. *Sci. Bull.* **2018**, *63*, 159−168.
(61) Wu, B.; Liu, X.; Yin, J.; Lee, H. Bulk β-Te to few layered β-tellurenes: indirect to direct band-Gap transitions showing semiconducting property. *Mater. Res. Express* **2017**, *4*, 095902.
(62) Chen, J.; Dai, Y.; Ma, Y.; et al. Ultrathin β-tellurium layers grown on highly oriented pyrolytic graphite by molecular-beam epitaxy. *Nanoscale* **2017**, *9*, 15945−15948.
(63) Huang, X.; Guan, J.; Lin, Z.; et al. Epitaxial Growth and Band Structure of Te Film on Graphene. *Nano Lett.* **2017**, *17*, 4619.
(64) Thupakula, U.; Laha, P.; Lippertz, G.; Schouteden, K.; Netsou, A.-M.; Seliverstov, A.; Terryn, H.; Pereira, L. M. C.; Van Haesendonck, C. Two-dimensional tellurium superstructures on Au(111) surfaces. *J. Chem. Phys.* **2022**, *157*, 164703.
(65) Huang, X.; Xiong, R.; Hao, C.; Li, W.; Sa, B.; Wiebe, J.; Wiesendanger, R. Experimental Realization of Monolayer α-Tellurene. *Adv. Mater.* **2024**, *36*, 2309023.
(66) Jnawali, G.; Xiang, Y.; Linser, S. M.; Shojaei, I. A.; Wang, R.; Qiu, G.; Lian, C.; Wong, B. M.; Wu, W.; Ye, P. D.; Leng, Y.; Jackson, H. E.; Smith, L. M. Ultrafast photoinduced band splitting and carrier dynamics in chiral tellurium nanosheets. *Nat. Commun.* **2020**, *11*, 3991.
(67) Xie, Z.; Xing, C.; Huang, W.; Fan, T.; Li, Z.; Zhao, J.; Xiang, Y.; Guo, Z.; Li, J.; Yang, Z.; Dong, B.; Qu, J.; Fan, D.; Zhang, H. Ultrathin 2d nonlayered tellurium nanosheets: facile liquid-phase exfoliation, characterization, and photoresponse with high performance and enhanced stability. *Adv. Funct. Mater.* **2018**, *28*, 1705833.
(68) Peierls, R. E. *Quantum Theory of Solids*; Oxford University Press: New York, 1955.
(69) Zhu, X.; et al. Classification of charge density waves based on their nature. *Proc. Natl. Acad. Sci. U.S.A.* **2015**, *112*, 2367−2371.
(70) Kwok, R. S.; Brown, S. E. Thermal conductivity of the charge-density-wave systems $K_{0.3}MoO_3$ and $(TaSe_4)_2I$ near the Peierls transition. *Phys. Rev. Lett.* **1989**, *63*, 895.
(71) De Sorbo, W. J. Concerning the Low Temperature Specific Heat of Tellurium. *J. Chem. Phys.* **1953**, *21*, 764.
(72) Loferski, J. J. Infrared Optical Properties of Single Crystals of Tellurium. *Phys. Rev.* **1954**, *93*, 707.
(73) Nomura, C. Optical activity in tellurium. *Phys. Rev. Lett.* **1960**, *5*, 500.
(74) Cherin, P.; Unger, P. Two-dimensional refinement of the crystal structure of tellurium. *Acta Crystallogr.* **1967**, *23*, 670−671.

https://doi.org/10.1021/acs.nanolett.5c01695
Nano Lett. XXXX, XXX, XXX−XXX